



# Modelling present-day basal melt rates for Antarctic ice shelves using a parametrization of buoyant meltwater plumes

Werner M. J. Lazeroms<sup>1</sup>, Adrian Jenkins<sup>2</sup>, G. Hilmar Gudmundsson<sup>2</sup>, and Roderik S. W. van de Wal<sup>1</sup>

<sup>1</sup>Institute for Marine and Atmospheric Research Utrecht, Utrecht University, Utrecht, The Netherlands

<sup>2</sup>British Antarctic Survey, Natural Environment Research Council, Cambridge, United Kingdom

*Correspondence to:* Werner M. J. Lazeroms (w.m.j.lazeroms@uu.nl)

**Abstract.** Basal melting below ice shelves is a major factor in the decline of the Antarctic ice sheet, which can contribute significantly to possible future sea-level rise. Therefore, it is important to have an adequate description of the basal melt rates for use in ice-dynamical models. Most current ice models use rather simple parametrizations based on the local balance of heat between ice and ocean. In this work, however, we use a recently derived parametrization of the melt rates based on a buoyant plume travelling upward beneath an ice shelf. This plume parametrization combines a nonlinear ocean temperature sensitivity with an inherent geometry dependence, which is mainly described by the grounding-line depth  $z_{gl}$  and the local slope  $\alpha$  of the ice-shelf base. For the first time, this type of parametrization is evaluated on a two-dimensional grid covering the entire Antarctic continent. In order to apply the essentially one-dimensional parametrization to realistic ice-shelf geometries, we present an algorithm that determines effective values for  $z_{gl}$  and  $\alpha$  for any point beneath an ice shelf. Furthermore, since detailed knowledge of temperatures and flow patterns in the ice-shelf cavities is sparse or absent, we construct an effective ocean temperature field from observational data with the purpose of matching (area-averaged) melt rates from the model with observed present-day melt rates. The result is a realistic map of basal melt rates around Antarctica, not only in terms of average values, but also in terms of the spatial pattern, with high melt rates typically occurring near the grounding line. The plume parametrization and the effective temperature field are therefore promising tools for future simulations of the Antarctic ice sheet.

## 1 Introduction

The Antarctic ice sheet is characterized by vast areas of floating ice at its margins, comprising ice shelves, both large and small, that buttress the outflow of ice from inland. The stability of these ice shelves is governed by a delicate mass balance, consisting of an influx of ice from the glaciers, iceberg calving at the ice front, snowfall and ablation at the surface, and basal melting due to the flow of ocean water in the ice-shelf cavities. Recent studies suggest that Antarctic ice shelves are experiencing rapid thinning (Pritchard et al., 2009, 2012; Paolo et al., 2015), an effect which can be traced back to an increase in basal melting (Depoorter et al., 2013; Rignot et al., 2013). This is especially apparent in West Antarctica, where relatively warm ocean water in the Amundsen and Bellingshausen seas is able to flow into the ice-shelf cavities and enhance melting from below. Increased basal melt rates and thinning of ice shelves decrease the buttressing effect, enhancing the ice flow and associated mass loss



from the Antarctic glaciers and ice sheet. This can significantly affect future sea-level rise, as suggested by recent numerical simulations (Golledge et al., 2015; Ritz et al., 2015; DeConto and Pollard, 2016).

In view of these issues, it is necessary to have accurate models of the dynamics of ice shelves, in which basal melting at the interface between ice and ocean plays an important role. State-of-the-art ice-sheet models for large-scale climate simulations 5 (see e.g. De Boer et al. 2015) provide a complete description of the flow and thermodynamics of ice. Due to the complex nature of the system and high computational cost of climate simulations, these models inevitably contain approximations and parametrizations of many physical processes, among which basal melting is no exception. In particular, it is challenging to resolve the ocean dynamics within the ice-shelf cavities at a continental scale, which severely restricts the level of detail possible in basal melt parametrizations. These parametrizations can be as simple as constant values or depend solely on the thickness 10 of the water column beneath the ice shelf. However, most recent simulations (e.g. De Boer et al. 2015; DeConto and Pollard 2016) determine the basal melt rate from a steady-state heat flux at the ice-ocean interface (Beckmann and Goosse, 2003), driven by a far-field temperature and a number of tuning factors.

As demonstrated by observational data (e.g. Rignot et al. 2013), the basal melt rates around Antarctica show a complex spatial pattern, which depends heavily on both the geometry below the ice shelves and the ocean temperature. Due to their 15 steady nature, it is unlikely that the simple basal melt parametrizations contain enough physical details to capture this complex pattern without either significant tuning or extremely detailed ocean-shelf-cavity models. On the other hand, the ocean dynamics and associated melt rates within a single ice-shelf cavity have been studied in rather high detail in recent years. For example, Holland et al. (2008) showed that basal melt rates obtained from a general ocean circulation model respond quadratically to changing ocean temperatures. These studies shed light on the minimal requirements of basal melt parametrizations, 20 i.e. a nonlinear temperature sensitivity, an inherent geometry dependence corresponding to the unresolved ocean circulation, and a depth-dependent pressure freezing point, yielding higher melt rates at greater depths and the possibility of refreezing at lesser depths.

Therefore, we develop here a more advanced parametrization for the basal melt rates, based on the theory of buoyant meltwater plumes, which was first applied to the ice-shelf cavities by MacAyeal (1985). In this theory, it is assumed that the 25 main physical mechanism driving the ocean circulation within the cavity is the positive buoyancy of meltwater, which travels upward beneath the ice-shelf base in the form of a turbulent plume. Melting at the ice-ocean interface is influenced by the fluxes of heat and meltwater through the ocean boundary layer, which depend on the plume dynamics. The upward motion of the plume induces an inflow of possibly warmer ocean water into the ice shelf cavity, creating more melt. Entrainment from the surrounding ocean water affects the momentum and thickness of the plume as it moves up the ice-shelf base. Depending 30 on the stratification of the ocean water inside the cavity, the plume may reach a level of neutral buoyancy from which it is no longer driven upward.

All these physical processes can be captured by a quasi-one-dimensional model of the mass, momentum, heat and salt fluxes within the plume and are shown schematically in Fig. 1. In particular, this work is based on the plume model of Jenkins (1991), 35 from which a basal melt parametrization has recently been derived (Jenkins, 2011, 2014). This parametrization is based on an empirical scaling of the plume model results in terms of ambient ocean properties and the geometry of the ice-shelf cavity. The



geometry dependence is mainly determined by the grounding-line depth and the slope of the ice-shelf base. The aim of this particular study is to apply the plume parametrization to a two-dimensional grid covering all of Antarctica, in order to investigate if this type of parametrization is able to give realistic present-day values and capture the complex pattern of basal melt rates shown in observations (Rignot et al., 2013).

5 In the following section, we describe the details of the plume model and the basal melt parametrization derived from it (Sections 2.1 and 2.2). An important part of the work is an algorithm that translates the parametrization from a one-dimensional to a two-dimensional geometry, as described in Section 2.3. In Section 3.1, we show results from the numerical evaluation of the (still 1-D) parametrization along flow lines of two well-known Antarctic ice shelves, namely Filchner-Ronne and Ross. Finally, Sections 3.2 and 3.3 discuss the application of the 2-D plume parametrization to the entire Antarctic continent, resulting in a two-dimensional map of basal melt rates under the ice shelves. Special attention is given to the construction of an effective ocean temperature field from observations, which is required for providing realistic input data of the temperature within the ice-shelf cavities to the parametrization. The results are compared with those from simple heat-balance models (Beckmann and Goosse, 2003; DeConto and Pollard, 2016).

## 2 Modelling basal melt

15 In this section, we start with a description of the basic physics underlying basal melt models. We summarize the quasi-one-dimensional plume model of (Jenkins, 1991) and the development of the plume parametrization (Jenkins, 2011, 2014) resulting from this model. In particular, we discuss the method used to extend this plume parametrization to two-dimensional input data, necessary for use in a fully functional ice-dynamical model.

First of all, we briefly discuss a common feature of many basal melt parametrizations, namely the dependence on the 20 local balance of heat at the ice-ocean interface. In its simplest form, this is a balance between the latent heat of fusion and the heat flux through the sub-ice-shelf boundary layer, which can be expressed as follows (Holland and Jenkins, 1999; Beckmann and Goosse, 2003):

$$\rho_i \dot{m} L = \rho_w c_w \gamma_T (T_a - T_f), \quad (1a)$$

where  $\rho_i, \rho_w$  are the densities of ice and water, respectively,  $\dot{m}$  is the melt rate,  $L$  is the latent heat of fusion for ice,  $c_w$  is the 25 specific heat capacity of the ocean water,  $\gamma_T$  is a turbulent exchange velocity and  $T_a$  is the temperature of the ambient ocean water. In this model, the melting is driven by the difference between  $T_a$  and the depth-dependent freezing point,

$$T_f = \lambda_1 S_w + \lambda_2 + \lambda_3 z_b, \quad (1b)$$

where  $S_w$  is salinity of the surrounding ocean,  $z_b$  is the depth of the ice-shelf base, and  $\lambda_1, \lambda_2, \lambda_3$  are constant parameters. As explained by Holland and Jenkins (1999), more details can be included in this basal melt model, e.g. heat conduction into the ice 30 and a balance equation for salinity (see also Section 2.1). Nevertheless, many ice models contain basal melt parametrizations based on Eqs. (1) (see e.g. De Boer et al. 2015; DeConto and Pollard 2016). These models typically use either constant or

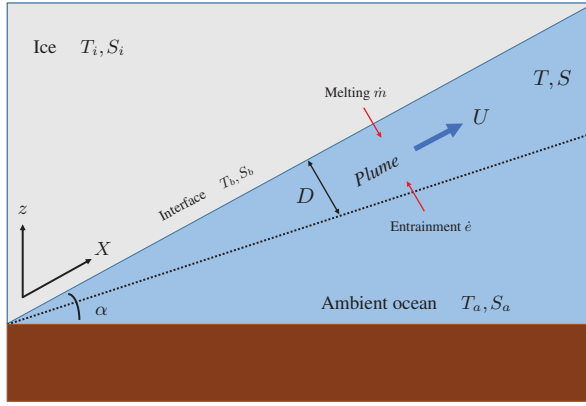


**Figure 1.** Schematic picture of the plume model. The plume travels upward under the ice-shelf base along the path  $X$  with speed  $U$  and thickness  $D$  while being influenced by melting and entrainment. Note that, in general, the slope angle  $\alpha$  can vary in the direction of  $X$ .

temperature dependent values for  $\gamma_T$ , leading to a melt rate that depends either linearly or quadratically on the temperature difference  $T_a - T_f$ . The latter case is consistent with the findings of Holland et al. (2008), who obtained a similar quadratic relationship from the output of an ocean general circulation model applied to the ice-shelf cavities. The non-linearity arose because the exchange velocity  $\gamma_T$  in Eq. (1a) was expressed as a linear function of the ocean current driving mixing across the

5 boundary layer.

Hence, the exchange velocity plays an important role in correctly determining the heat balance at the ice-ocean interface, or, more precisely, the heat transfer through the ocean boundary layer beneath the ice shelves. However, a local heat-balance model as expressed by (1) is too simplistic to capture the effects of the ocean circulation on the basal melting, e.g. those depending on the ice-shelf geometry. The plume model and parametrization discussed in the remainder of this section are considered the 10 next step in modelling the physics for general ice-shelf geometries without having to rely on full ocean circulation models, for which there are also insufficient input data to obtain a universal Antarctic solution.

## 2.1 Plume model

The parametrization used in this study is ultimately based on the plume model developed by Jenkins (1991). Here we summarize the key assumptions and physics behind this model. The ice-shelf cavity is modelled by a two-dimensional geometry 15 (Fig. 1), in which the ice-shelf base has a (local) slope given by the angle  $\alpha$ . This geometry is assumed to be uniform in the direction perpendicular to the plane and constant in time and can be seen as a vertical cross-section along a flow line of the ice shelf. We can define a coordinate  $X$  along the ice-shelf base with slope  $\alpha$  and consider the development of a meltwater plume initiating at the grounding line ( $X = 0$ ) and moving up along the ice-shelf base due to positive buoyancy with respect to the ambient ocean water.



The situation depicted in Fig. 1 essentially yields a two-layer system of the meltwater plume with varying thickness  $D$ , velocity  $U$ , temperature  $T$  and salinity  $S$  lying above the ambient ocean with temperature  $T_a$  and salinity  $S_a$ . As explained in Jenkins (1991), the typically small values of the slope angle  $\alpha$  allow us to consider conservation of mass, momentum, heat and salt within the plume in a depth-averaged sense. Moreover, as the plume travels upward in the direction of  $X$ , it is affected by 5 entrainment (at rate  $\dot{e}$ ) of ambient ocean water, as well as the fluxes of meltwater (with melt rate  $\dot{m}$ ) and heat at the ice-ocean interface (with temperature  $T_b$  and salinity  $S_b$ ). These considerations yield the following quasi-one-dimensional system of equations for  $(D, U, T, S)$  as a function of the coordinate  $X$  along the shelf base, denoting the balance of mass, momentum, heat and salt within the plume:

$$\frac{dDU}{dX} = \dot{e} + \dot{m}, \quad (2a)$$

$$10 \quad \frac{dDU^2}{dX} = D \frac{\Delta\rho}{\rho_0} g \sin \alpha - C_d U^2, \quad (2b)$$

$$\frac{dDUT}{dX} = \dot{e} T_a + \dot{m} T_b - \Gamma_T U (T - T_b), \quad (2c)$$

$$\frac{dDUS}{dX} = \dot{e} S_a + \dot{m} S_b - \Gamma_S U (S - S_b), \quad (2d)$$

where  $g$  is the gravitational acceleration,  $C_d$  is the (constant) drag coefficient,  $\Delta\rho = \rho_a - \rho$  is the difference in density between plume and ambient ocean, and  $\Gamma_T, \Gamma_S$  are the turbulent exchange coefficients (Stanton numbers) of heat and salinity at the 15 ice-ocean interface. The above formulation makes explicit the linear dependence of the turbulent exchange velocities on the ocean current ( $\gamma_T = \Gamma_T U$ ,  $\gamma_S = \Gamma_S U$ ). The system of equations (2) is closed using suitable expressions for the entrainment rate  $\dot{e}$ , an equation of state  $\rho = \rho(T, S)$ , the balance of heat and salt at the ice-ocean interface and the liquidus condition. The expression for the entrainment rate is assumed to have the following form (Bo Pedersen, 1980):

$$\dot{e} = E_0 U \sin \alpha, \quad (3)$$

20 with  $E_0$  a dimensionless constant. Hence, the entrainment rate increases linearly with the plume velocity, is zero for a horizontal ice-shelf base, and grows with increasing slope angle. Furthermore, a linearized equation of state yields:

$$\frac{\Delta\rho}{\rho_0} = \beta_S (S_a - S) - \beta_T (T_a - T), \quad (4)$$

where  $\beta_S$  is the haline contraction coefficient and  $\beta_T$  the thermal expansion coefficient. The boundary conditions at the ice-ocean interface are given by:

$$25 \quad \Gamma_T U (T - T_b) = \dot{m} \left( \frac{L}{c_w} + \frac{c_i}{c_w} (T_b - T_i) \right), \quad (5a)$$

$$\Gamma_S U (S - S_b) = \dot{m} (S_b - S_i), \quad (5b)$$

$$T_b = \lambda_1 S_b + \lambda_2 + \lambda_3 z_b \quad (5c)$$

i.e. the first equation balances the turbulent exchange of heat with heat conduction and latent heat of fusion  $L$  in the ice, where  $c_w$  and  $c_i$  are the specific heat capacities of seawater and ice, respectively, and  $T_i$  is the ice temperature. Similarly, Eq. (5b) is



a balance between turbulent exchange of salt and diffusion into the ice. Eq. (5c) is the (linearized) liquidus condition that puts the interface temperature equal to the pressure freezing point at the local depth  $z_b$  of the ice-shelf base, similar to Eq. (1b).

Equations (2)-(5) form a closed set that can be solved to obtain the prognostic variables ( $D, U, T, S$ ) of the plume as a function of the plume path  $X$ , given the ice-shelf draft  $z_b(X)$  with slope angle  $\alpha(X)$ , the ambient ocean properties  $T_a(z)$  and  $S_a(z)$ , and the ice properties  $T_i$  and  $S_i$ . Of particular interest for the current work, however, are the ice-ocean interface conditions (5), which essentially determine the melt rate  $\dot{m}$ , the key quantity of this study. In other words, the melt rate is determined by the fluxes of heat and salt at the interface, which in turn are linked to the development of the plume. Note that these boundary conditions can be simplified (McPhee, 1992; McPhee et al., 1999) to only two equations containing the freezing temperature  $T_f$  of the plume, rather than the interface properties  $T_b$  and  $S_b$ :

$$10 \quad \Gamma_{TS}U(T - T_f) = \dot{m} \left( \frac{L}{c_w} + \frac{c_i}{c_w}(T_f - T_i) \right), \quad (6a)$$

$$T_f = \lambda_1 S + \lambda_2 + \lambda_3 z_b, \quad (6b)$$

where  $\Gamma_{TS}$  is an effective heat exchange coefficient. This simplified formulation can be used together with the prognostic equations (2) by assuming  $T_b = T_f$ , whereas  $S_b$  disappears from the problem by substituting (5b) in (2d). As shown by Jenkins et al. (2010), both Eqs. (5) and Eqs. (6) give similar results when used to describe basal melt rates under Ronne Ice Shelf. Also note 15 the similarity between Eqs. (6) and the simple melt model described by Eqs. (1), the difference being the inclusion of heat conduction and the parametrization  $\gamma_T = \Gamma_{TS}U$ . Hence, the turbulent exchange in this model is directly determined by the plume velocity that appears as a prognostic variable.

Without giving further details, we mention that the plume model described above can be evaluated for different ice-shelf geometries (i.e. vertical cross-sections along flow lines) and different vertical temperature and salinity profiles of the ambient 20 ocean (Jenkins, 2011, 2014). In this model, the general physical mechanism governing the development of the plume is the addition of meltwater at the ice-ocean interface, which increases its buoyancy. Changes in buoyancy affect plume speed and that, combined with its temperature and salinity, determines the subsequent input of meltwater.

## 2.2 Basal melt parametrization along a flow line

Evaluating the aforementioned plume model for different geometries and ocean properties leads to a wide variety of solutions 25 for the basal melt rates. The question arises whether there exists an appropriate scaling with external parameters that combines these results into a universal melt pattern. Here we will summarize how such a scaling can be found, leading to the basal melt parametrization of Jenkins (2014) for the quasi-one-dimensional geometries along flow lines described in the previous section. Section 2.3 will discuss the extension of this parametrization to more realistic two-dimensional geometries.

A general solution to the problem is challenging to find as there are at least four length scales that determine the plume 30 evolution (Jenkins, 2011). The first governing length scale is associated with the pressure dependence of the freezing point that imposes an external control on the relationship between plume temperature, plume salinity and the melt rate, which is determined by the temperature relative to the freezing point. Lane-Serff (1995) discussed how this length scale determines the distribution of melting and freezing beneath an ice shelf. The second length scale is associated with the ambient stratification,



which determines how far the plume can rise before reaching a level of neutral buoyancy. Magorrian and Wells (2016) discuss the plume behaviour and resulting melt rates when this length scale dominates. Critically, with the pressure dependence of the freezing point assumed to be negligible, as required in the analysis of Magorrian and Wells (2016), no freezing can occur. A third length scale can be formulated by comparing the input of buoyancy from freshwater outflow at the grounding line with 5 the input of buoyancy by melting at the ice-ocean interface (Jenkins, 2011). This length scale indicates the size of the zone next to the grounding line where the impact of ice shelf melting on plume buoyancy can be ignored and conventional plume theory (Morton et al., 1956; Ellison and Turner, 1959) applied, and is generally small compared with typical ice shelf dimensions. A final length scale is that at which the Coriolis force takes over from friction as the primary force balancing the plume buoyancy 10 in the momentum budget. Jenkins (2011) discussed the three larger length scales in the context of which would take over as the dominant control on plume behaviour beyond the initial zone near the grounding line where the initial source of buoyancy dominates, and showed the length scale associated with the pressure dependence of the freezing point to be most important for typical ice-shelf conditions.

Hence, in order to obtain a universal curve for the melt rate beneath an ice shelf, Jenkins (2014) extended the analysis of Lane-Serff (1995), who showed how the length scale defined by:

$$15 \quad L = \frac{T_a - T_f}{\lambda_3} \quad (7)$$

approximately determined the zones of melting and freezing produced by the plume. The variation in the transition point from melting to freezing is a function of the ice-shelf basal slope. As discussed by Jenkins (2011), the slope affects the entrainment rate, but not the melt rate, so there is a geometrical factor that scales the elevation of the plume temperature above the local freezing point:

$$20 \quad \frac{E_0 \sin \alpha}{\Gamma_{TS} + E_0 \sin \alpha}. \quad (8)$$

Using this factor, a universal length scale can be empirically derived (Appendix A). Note that Jenkins (2011) simplified the plume model by using (6) directly, whereas Jenkins (2014) retained the more complex melt formulation (5) in the model while seeking empirical scalings based on an effective  $\Gamma_{TS}$ . As discussed by Holland and Jenkins (1999), the factor relating  $\Gamma_T$  and  $\Gamma_{TS}$  is itself a function of the plume temperature, so Jenkins (2014) expressed the effective  $\Gamma_{TS}$  as an empirical function of 25  $\Gamma_T$ , (7) and (8) (see Appendix A). When distance along the plume path is scaled with this slightly more complex factor (see Eq. (A4)), the melt rates produced by the plume model conform to a universal form, first rising to a peak at the same scaled distance, before falling and transitioning to freezing at a common point.

With the distance along the plume path appropriately scaled, all that remains is to scale the amplitude of the curves. As in Jenkins (2011) the appropriate physical scales are: 1) the temperature of the ambient seawater relative to the freezing point; 30 2) the factor in Eq. (8) scaling the temperature elevation of the plume above freezing; 3) a factor that scales the plume speed, given by the ratio of plume buoyancy to frictional drag:

$$\left( \frac{\sin \alpha}{C_d + E_0 \sin \alpha} \right) \left( \frac{\Gamma_{TS}}{\Gamma_{TS} + E_0 \sin \alpha} \right). \quad (9)$$

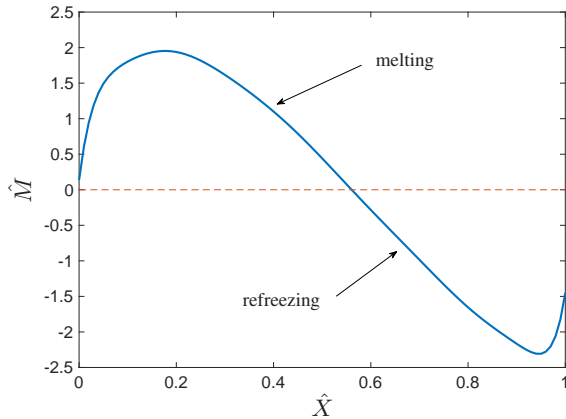


**Figure 2.** Dimensionless melt curve  $\hat{M}(\hat{X})$  used in the basal melt parametrization. Higher melt rates typically occur close to the grounding line with a maximum at  $\hat{X} \approx 0.2$ . A transition from melting to refreezing may occur further away from the grounding line, depending on the position of the ice front. Note that the value of  $\hat{X}$  depends on the distance to the grounding line, as well as the temperature difference  $T_a - T_f$  and the local slope  $\alpha$  (see Appendix A). In other words,  $\hat{X} = 0$  corresponds to the grounding line, but the dimensionless position of the ice-shelf front depends on the length scale and is not necessarily equal to  $\hat{X} = 1$ .

The second term in parenthesis is the factor that scales the plume temperature relative to the ambient temperature and thus controls plume buoyancy. It replaces the initial buoyancy flux at the grounding line used in the scaling of Jenkins (2011). The final expression includes factors and powers that are derived empirically to yield an approximately universal melt rate curve, which can then be represented by a single polynomial expression that is accurate to about 20% for melt rates ranging over 5 many orders of magnitude (Jenkins, 2014).

In application, the basal melt parametrization thus consists of a general expression for the dimensionless melt rate  $\hat{M}$  as a function of the dimensionless coordinate  $\hat{X}$  measured from the grounding line (Fig. 2). This dimensionless coordinate is essentially the depth difference  $z_b - z_{gl}$  scaled by a temperature- and depth-dependent length scale. Hence,  $\hat{X} = 0$  corresponds to the grounding line and any shelf point downstream from the grounding line corresponds to a value  $0 < \hat{X} < 1$  depending on 10  $T_a$  and  $\alpha$ . This scaling also implies that the edge of the ice shelf is not necessarily located at  $\hat{X} = 1$ , but its location is highly dependent on the input variables. In summary, to obtain the basal melt rate  $m$  at any point beneath the ice-shelf, one requires the local depth  $z_b$ , local slope  $\alpha$ , grounding-line depth  $z_{gl}$  and ambient ocean properties  $T_a$  and  $S_a$  to determine the corresponding value on the dimensionless curve  $\hat{M}(\hat{X})$ , which then has to be multiplied by the physical scales given in Appendix A. The physical quantities and constant parameters required for evaluating the parametrization are summarized in Table 1.

### 15 2.3 Basal melt parametrization in 2-D: effective plume path

As explained in the previous section, an important feature of the basal melt parametrization is its dependence on non-local quantities, in particular the grounding-line depth  $z_{gl}$  from which the plume originated. Therefore, in order to apply the parametriza-



**Table 1.** Physical quantities and constant parameters serving as input for the basal melt parametrization.

External quantities		Units
$z_b$	Local depth of ice-shelf base	m
$\alpha$	Local slope angle	—
$z_{gl}$	Depth of grounding line	m
$T_a$	Ambient ocean temperature	°C
$S_a$	Ambient ocean salinity	psu
Constant parameters		Values
$E_0$	Entrainment coefficient	$3.6 \times 10^{-2}$
$C_d$	Drag coefficient	$2.5 \times 10^{-3}$
$\Gamma_T$	Turbulent heat exchange coefficient	$1.1 \times 10^{-5}$
$\Gamma_{TS0}$	Effective heat exchange coefficient	$6.0 \times 10^{-4}$
$\lambda_1$	Freezing point-salinity coefficient	$-5.73 \times 10^{-2}$ °C
$\lambda_2$	Freezing point offset	$8.32 \times 10^{-2}$ °C
$\lambda_3$	Freezing point-depth coefficient	$7.61 \times 10^{-4}$ K m <sup>-1</sup>

tion to realistic geometries, one needs to know for each ice-shelf point the corresponding grounding-line point(s) serving as the origin of the plume(s) reaching that particular shelf point. For the quasi-one-dimensional settings considered so far, this is not an issue, since the plume can only travel in one direction. However, for general ice-shelf cavities, an arbitrary shelf point can be reached by plumes from multiple directions, corresponding not only to different values for  $z_{gl}$ , but also to different slope angles  $\alpha$ . This means that the plume parametrization cannot be directly applied to such geometries. An algorithm is needed to determine effective values for  $z_{gl}$  and  $\alpha$ , which is discussed below. Note that this algorithm is not unique; an alternative method with slightly different results is discussed in Appendix B.

As a starting point, we consider the usual topographic data in terms of two-dimensional fields for the ice thickness  $H_i$ , bedrock elevation  $H_b$  and surface elevation  $H_s$  used by ice-dynamical models. In this study, we use remapped data based on the Bedmap2 dataset for Antarctica (Fretwell et al., 2013), but the following algorithm is valid for any topographic data on a rectangular grid with any resolution  $\Delta x \times \Delta y$ . First of all, the topographic data are used to define an ice mask based on the criterion for floating uniform ice, as shown in Table 2. Furthermore, the depth of the ice base is easily determined to be:

$$z_b = H_s - H_i. \quad (10)$$

Now, in order to apply the basal melt parametrization to this two-dimensional data, we must determine effective values for  $z_{gl}$  and  $\alpha$  for every *ice-shelf* point  $(i, j)$  with basal depth  $z_b(i, j)$ , where the indices  $i$  and  $j$  denote the position on the grid. This is done by first searching for "valid" grounding-line points in 16 directions on the grid, starting from *any* shelf point  $(i, j)$ , as



**Table 2.** Definition of the ice mask. The ice-shelf criterion is that for uniform ice with density  $\rho_i$  floating on ocean water with density  $\rho_w$ . The minimum ice thickness used here is  $H_{i,\min} = 2$  m.

Mask value	Type	Criterion
0	ice sheet	$(\rho_i/\rho_w)H_i > -H_b$
1	ice shelf	$(\rho_i/\rho_w)H_i \leq -H_b$
2	ocean / no ice	$H_i \leq H_{i,\min}$

depicted in Fig. 3a. Note that we can calculate a local basal slope  $s_n(i, j)$  at the point  $(i, j)$  in the  $n$ -th direction as follows:

$$s_n(i, j) = \frac{z_b(i, j) - z_b(i + i_n, j + j_n)}{\sqrt{(i_n \Delta x)^2 + (j_n \Delta y)^2}}, \quad (11)$$

where  $(i_n, j_n)$  denotes a direction vector on the grid, i.e.  $(i_n, j_n) = (1, 0)$  denotes right,  $(i_n, j_n) = (0, 1)$  denotes up, etc., and  $\Delta x$  and  $\Delta y$  denote the horizontal grid size in the  $x$ - and  $y$ -direction, respectively. To determine whether a grounding-line point 5 found in one of the 16 directions is valid for the calculation of the basal melt, we apply the following two criteria:

1. Assuming that a buoyant meltwater plume can only reach the point  $(i, j)$  from the  $n$ -th direction if the basal slope in that direction is positive, we only search in directions for which  $s_n(i, j) > 0$ .

2. If the first criterion is met for the  $n$ -th direction, the algorithm searches in this direction for the nearest *ice-sheet* point.

This point is only considered to be a valid grounding-line point if it lies deeper than the original ice-shelf point at  $(i, j)$ , 10 assuming again that a buoyant meltwater plume from the grounding line can only go up. Note, however, that we can obtain a better estimate of the true grounding-line depth in this direction, say  $d_n(i, j)$ , if we interpolate along either the bed or the ice base, as shown in Fig. 3b and c. The second criterion then becomes  $d_n(i, j) < z_b(i, j)$ .

Following the above procedure yields for each ice-shelf point  $(i, j)$  a set of grounding-line depths  $d_n$  and local slopes  $s_n$  in the directions that are "valid" according to the aforementioned two criteria. Mind that not all directions may yield a (valid) 15 grounding-line point, in particular those towards the open ocean. Now, in order to determine the *effective grounding-line depth*  $z_{gl}(i, j)$  and *effective slope angle*  $\alpha(i, j)$  necessary for calculating the basal melt in the shelf point  $(i, j)$ , we simply take the average of the found values for  $d_n$  and  $s_n$ :

$$z_{gl}(i, j) = \frac{1}{N_{ij}} \sum_{\text{valid } n} d_n(i, j), \quad (12a)$$

$$\tan[\alpha(i, j)] = \frac{1}{N_{ij}} \sum_{\text{valid } n} s_n(i, j), \quad (12b)$$

20 where  $N_{ij}$  denotes the number of valid directions found for the shelf point  $(i, j)$ . On the other hand, if no valid values for  $d_n$  and  $s_n$  are found for a particular shelf point, we take  $z_{gl} = z_b$  and  $\alpha = 0$ , leading to zero basal melt in that point (see Appendix A).

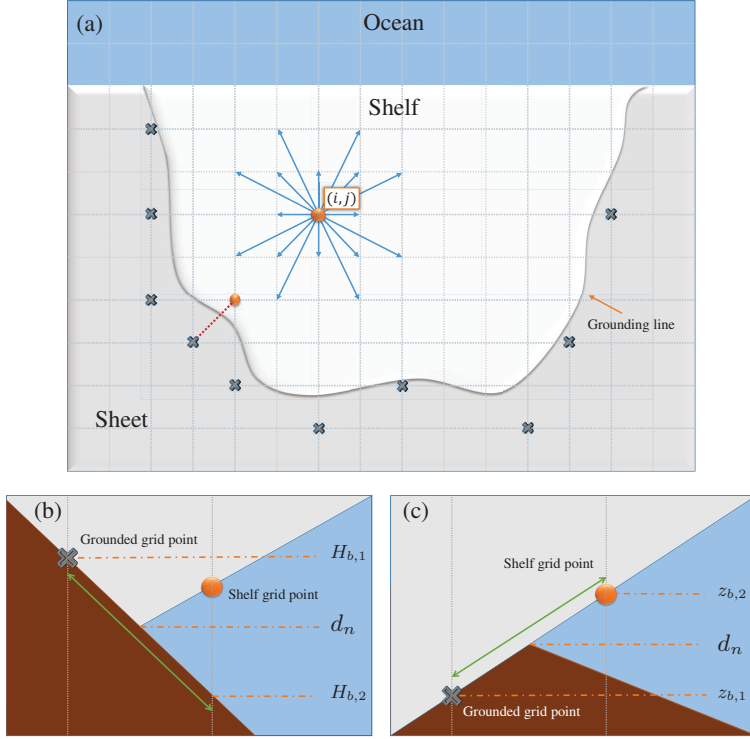


**Figure 3.** Schematic of the algorithm for finding the average grounding-line depth and associated slope angle used by the basal melt parametrization. (a) Top view of an ice-shelf on a horizontal grid. The algorithm searches in 16 directions from the shelf point  $(i, j)$ . Possible grounded points found in this way are marked by  $\times$ . (b) Vertical slice along the  $n$ -th direction (e.g. the red dotted line in (a)). If the grounded point is higher than the previous shelf point, the grounding-line depth  $d_n$  is found by interpolation along the bed ( $d_n = \frac{1}{2}(H_{b,1} + H_{b,2})$ ). (c) Interpolation along the ice base if the grounded point in the  $n$ -th direction is deeper than the previous shelf point ( $d_n = \frac{1}{2}(z_{b,1} + z_{b,2})$ ).

In summary, the method described above yields two-dimensional fields for the effective grounding-line depth  $z_{gl}$  and effective slope  $\tan(\alpha)$ , given topographic data in terms of  $H_i$ ,  $H_s$  and  $H_b$  and a suitable ice mask, such as the one defined in Table 2. These fields, in turn, serve as input for the basal melt parametrization described in the previous section, together with appropriate data for the ocean temperature  $T_a$  and salinity  $S_a$  (discussed in Section 3.2). We thus obtain a complete method 5 for calculating the basal melt for all Antarctic ice shelves, given the topography and ocean properties, which can also be used in conjunction with ice-dynamical models. In the following, however, we use the Bedmap2 dataset (Fretwell et al., 2013) to define the present-day topography of Antarctica and disregard the ice dynamics. More specifically, the original Bedmap2 data is remapped to a rectangular grid with grid size  $\Delta x = \Delta y = 20$  km, using the mapping package OBLIMAP 2.0 (Reerink et al., 2016). The resulting topographic data can be used as input for the algorithm described here, leading to the fields for  $z_{gl}$  and 10  $\tan(\alpha)$  shown in Fig. 4, which are used for the basal melt calculations discussed in Section 3. In Fig. 4b one can see that the

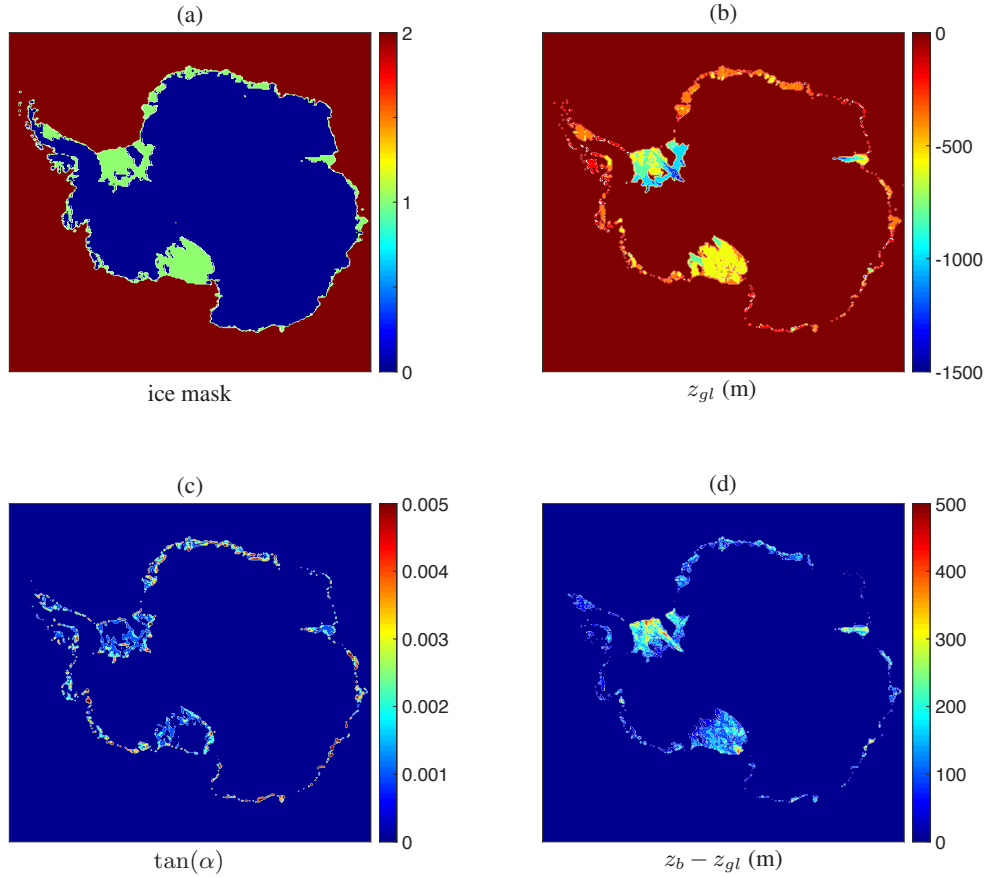


**Figure 4.** Effective plume paths under the Antarctic ice shelves as calculated by the algorithm of Section 2.3 using the Bedmap2 topographic data remapped on a 20 km by 20 km grid. (a) Ice mask according to Table 2. (b) The effective grounding-line depth  $z_{gl}$ . (c) The effective slope  $\tan(\alpha)$ . (d) The difference between local ice-base depth and associated grounding-line depth,  $z_b - z_{gl}$ .

lowest values of  $z_{gl}$  are obtained towards the inland regions of Filchner-Ronne ice shelf and Amery ice shelf. The values for the local slope are typically higher both near the grounding line and the ice front, as shown in Fig. 4c.

### 3 Results

Here we present various results obtained by evaluating the basal melt parametrization described in the previous section. First, 5 we investigate the main characteristics of the original 1-D parametrization of Section 2.2 by evaluating it along flow lines of the Filchner-Ronne and Ross ice shelves. In Sections 3.2 and 3.3, we turn to the full 2-D geometry of Antarctica using the



**Table 3.** Additional model parameters used for evaluating the plume model and the simple parametrizations described in Section 3.1.

Constant parameters		Values
$L$	Latent heat of fusion for ice	$3.35 \times 10^5 \text{ J kg}^{-1}$
$c_w$	Specific heat capacity of water	$3.974 \times 10^3 \text{ J kg}^{-1} \text{ K}^{-1}$
$c_i$	Specific heat capacity of ice	$2.009 \times 10^3 \text{ J kg}^{-1} \text{ K}^{-1}$
$\beta_S$	Haline contraction coefficient	$7.86 \times 10^{-4}$
$\beta_T$	Thermal expansion coefficient	$3.87 \times 10^{-5} \text{ K}^{-1}$
$g$	Gravitational acceleration	$9.81 \text{ m s}^{-2}$
$\rho_i$	Density of ice	$9.1 \times 10^2 \text{ kg m}^{-3}$
$\rho_w$	Density of ocean water	$1.028 \times 10^3 \text{ kg m}^{-3}$
$\gamma_T$	Turbulent exchange velocity (BG2003)	$5.0 \times 10^{-7} \text{ m s}^{-1}$
$\kappa_T$	Turbulent exchange coefficient (DCP2016)	$5.0 \times 10^{-7} \text{ m s}^{-1} \text{ K}^{-1}$

algorithm described in Section 2.3, first by constructing an appropriate effective ocean temperature field from observational data.

### 3.1 Comparison of basal melt parametrizations along flow lines

Topographic data along flow lines for both Filchner-Ronne ice shelf (FRIS) and Ross ice shelf are taken from Bombosch and Jenkins (1995) and Shabtaie and Bentley (1987), respectively. This data can be used to determine the quantities  $z_b$ ,  $\alpha$  and  $z_{gl}$  necessary for calculating the basal melt with the parametrization of Section 2.2. Furthermore, we define a uniform ambient ocean temperature  $T_a = -1.9 \text{ }^{\circ}\text{C} + \Delta T$ , where  $\Delta T$  is varied between runs, and a constant ambient ocean salinity  $S_a = 34.65 \text{ psu}$ . The results of these calculations are shown in Figs. 5 and 6 and compared with those of the full plume model described in Section 2.1. Moreover, we compare with two simple basal melt parametrizations based on Eqs. (1), namely the linear (i.e. in  $T_a - T_f$ ) parametrization by Beckmann and Goosse (2003) with constant  $\gamma_T$  and the quadratic parametrization by DeConto and Pollard (2016) with  $\gamma_T = \kappa_T |T_a - T_f|$ . Apart from the values listed in Table 1, additional model parameters used for these calculations are given in Table 3.

Figs. 5 and 6 show that both the current parametrization and the original plume model yield approximately the same melt-rate patterns as a function of the horizontal distance from the grounding line. These patterns roughly correspond to the dimensionless melt curve in Fig. 2, i.e. maximum melt near the grounding line and possibly refreezing further away along the flow line. This is most apparent in Fig. 5a, which clearly shows a transition from melting to freezing, since the relatively deep draft of FRIS allows higher values of the dimensionless coordinate  $\hat{X}$ . On the other hand, Fig. 6a does not show refreezing because the draft of Ross ice shelf is much shallower. Increasing the ocean temperature (through  $\Delta T$ ) can significantly enhance basal melt and remove the area of refreezing, as shown in Figs. 5b and 6b. In these cases, additional melt peaks occur in regions of high basal slope. Moreover, although the general agreement is good, the discrepancies between the current parametrization and

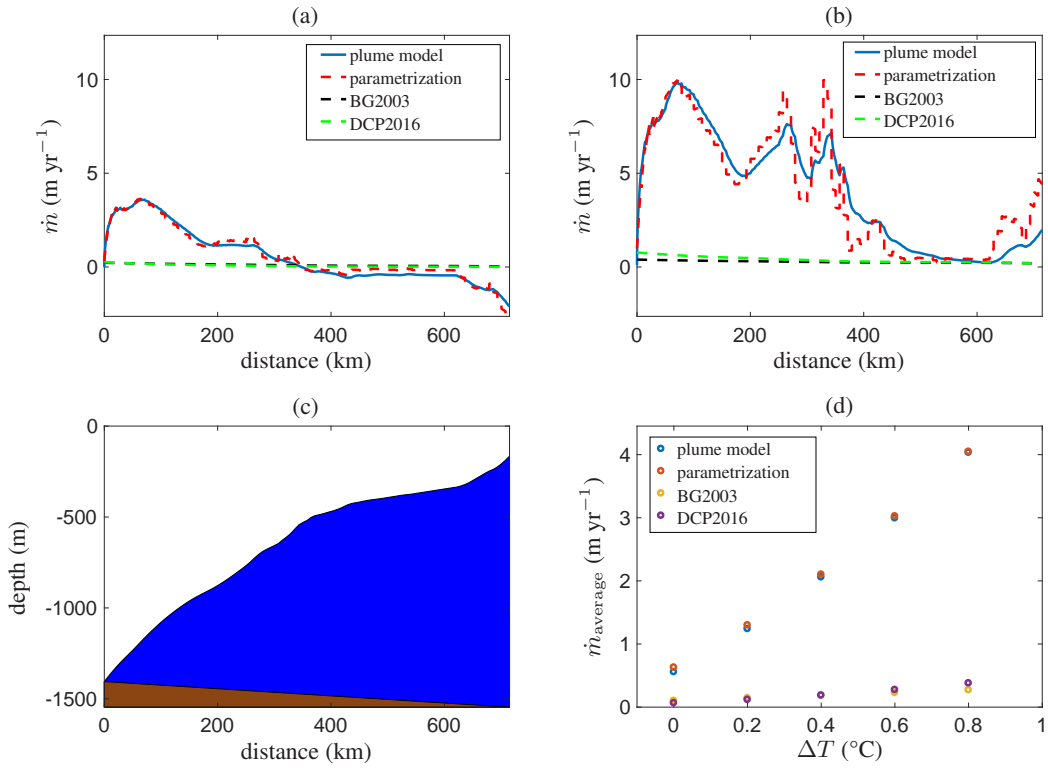


**Figure 5.** Comparison of the plume model (Section 2.1) with the 1-D basal melt parametrization (Section 2.2), as well as the parametrizations of Beckmann and Goosse (2003) (BG2003) and DeConto and Pollard (2016) (DCP2016), for a flow line along Filchner-Ronne ice shelf with uniform ocean temperature  $T_a = -1.9^\circ\text{C} + \Delta T$  and constant salinity  $S_a = 34.65 \text{ psu}$ . (a) Melt pattern for  $\Delta T = 0^\circ\text{C}$ . (b) Melt pattern for  $\Delta T = 0.8^\circ\text{C}$ . (c) Geometry of the ice-shelf base. (d) Horizontally averaged melt rates as a function of  $\Delta T$ .

the plume model are largest when the basal slope changes rapidly, because the parameterization responds immediately to the change while the full model has an inherent lag as the plume adjusts to the new conditions. On the whole, we see that the melt patterns given by the plume parametrization can be quite complex, while the two simple parametrization give nearly constant curves (i.e. independent of the position with respect to the grounding line).

5 It is interesting to investigate the temperature sensitivity of the four models in terms of the horizontally averaged melt rate as a function of  $\Delta T$ , as shown in Figs. 5d and 6d. In the case of FRIS, the plume model and parametrization are much more sensitive to the ocean temperature than the two simpler models. However, the average melt rates for Ross ice shelf are rather similar for all four models and all values of  $\Delta T$ . Hence, the difference in the temperature sensitivity depends significantly on the ice-shelf geometry, where the plume parametrization appears to have a larger potential for capturing diverse melt values than the simpler models. Note that in both cases, the temperature dependence of the plume parametrization is slightly 10 nonlinear, similar to the DeConto and Pollard (2016) parametrization, while the Beckmann and Goosse (2003) parametriza-

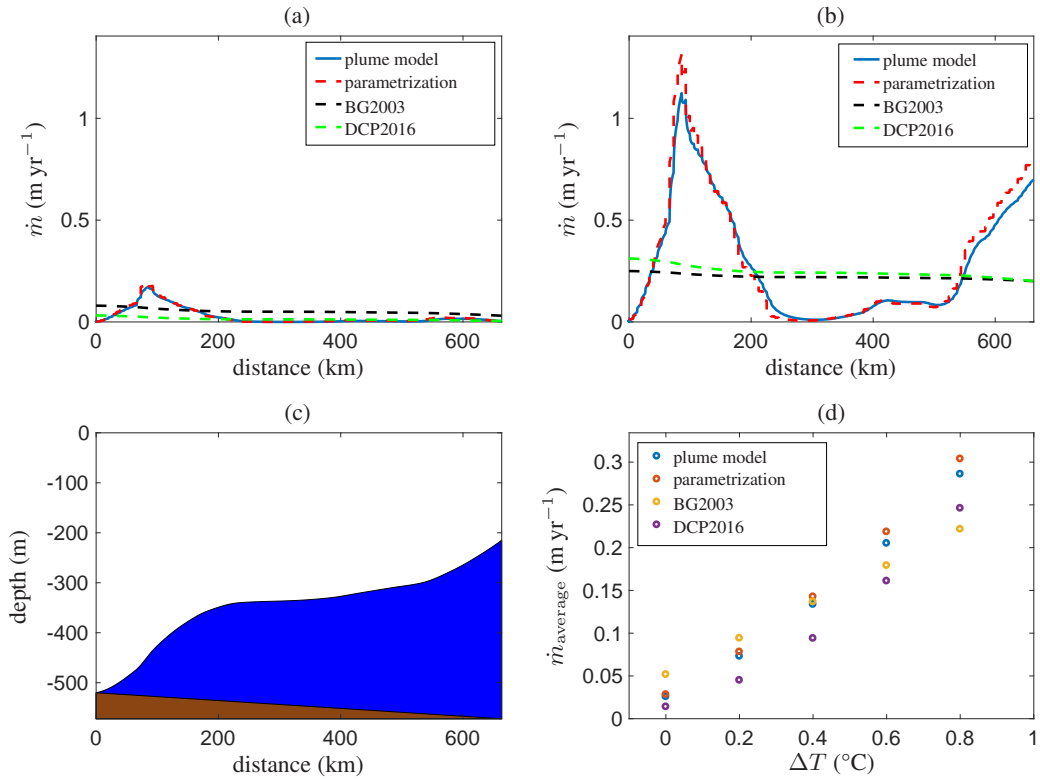


**Figure 6.** As Fig. 5, but for a flow line along Ross ice shelf.

tion has a linear temperature dependence. Following the discussion of Holland et al. (2008), the temperature dependence of the plume parametrization should therefore be more realistic than the one of Beckmann and Goosse (2003). However, the quadratic parametrization of DeConto and Pollard (2016) tends to underestimate the melt rates as well, despite its nonlinearity. It appears that the geometry dependence of the plume parametrization is an important factor for the temperature sensitivity of the calculated basal melt rates. In Section 3.3 we show that these geometrical effects are indeed crucial for obtaining realistic melt rates with the 2-D parametrization. This also means that the simplest basal melt parametrizations currently used in some ice-sheet models, namely constant values or monotonic functions of the water-column thickness below the ice shelf, are far from being valid. The latter class of models would even give a gradual increase of melt from the grounding line to the ice front, which is opposite to the behaviour of the plume parametrization in Figs. 5 and 6.

### 10 3.2 Effective ocean temperature

The previous section dealt with the 1-D basal melt parametrization along a flow line using a uniform ambient ocean temperature for the entire ice-shelf cavity. While a uniform temperature might appear a reasonable first approximation for a single ice shelf,

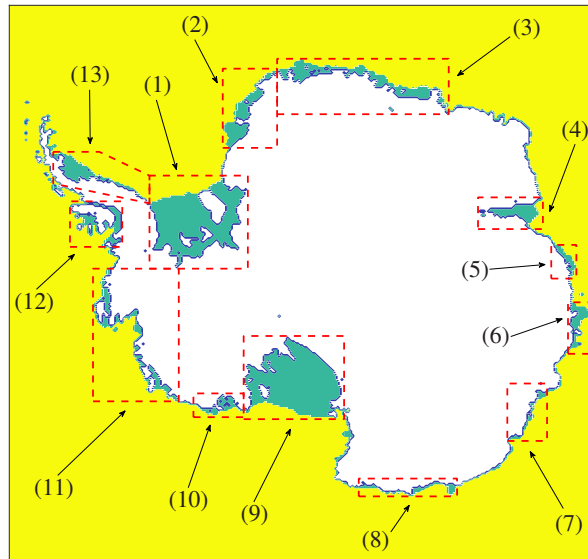


it is far from realistic to apply a single ocean temperature for multiple ice shelves around the entire Antarctic continent. Therefore, in order to apply the parametrization to the 2-D geometry defined by Fig. 4, a suitable 2-D field for the ocean temperature  $T_a$  is required. In principle, the same is true for the salinity  $S_a$ , but we will assume that the variations in ocean salinity around Antarctica are so small that the pressure freezing point  $T_f$  is only affected by variations in depth. In the 5 following, we will therefore take a uniform salinity  $S_a = 34.6$  psu.

Two problems arise when considering a 2-D ocean temperature field for forcing the parametrization. First of all, such a field should ideally be based on observational data, but ocean temperature measurements in the Antarctic ice-shelf cavities are sparse. The best possibility is an interpolated field based on ocean temperature data in the surrounding ocean, which 10 inevitably contains artefacts resulting from the non-uniform and predominantly summertime sampling. Secondly, even if a complete dataset of ocean temperatures were available, it is not immediately clear which temperatures (i.e. at which depth) are characteristic for the ocean water reaching the grounding lines (e.g. Jenkins et al. 2010). In principle, detailed knowledge 15 of the bottom topography and the ocean circulation would be required for this, which goes beyond the scope of the current modelling approach.

In view of these issues, we construct an *effective ocean temperature* field with which the current plume parametrization 20 yields melt rates that are as close as possible to present-day observations, averaged over entire ice shelves. This approach is based on the rationale that a model with a sufficiently realistic physical basis requires minimally tuned forcing data to produce realistic output. We shall shortly show that this is indeed possible with the plume parametrization. To determine whether the 25 resulting basal melt rates are realistic, we use the results of Rignot et al. (2013), who calculated the area-averaged melt rates for each Antarctic ice shelf, based on a combination of observational data and regional climate model output for the different terms in the local ice-shelf mass balance. Other datasets for recent Antarctic basal melt rates exist (e.g. Depoorter et al. 2013), as well as more recent data for ice-shelf thinning (Paolo et al., 2015) from which the basal melt rates can be calculated when 30 combined with the other terms in the mass balance (e.g. velocity and surface melt rates). These alternative datasets for the (area-averaged) basal melt rates are expected to be at least of the same order of magnitude, which we deem sufficient for the purpose of the current study. Since it is impossible to resolve each individual ice shelf from the Rignot et al. (2013) dataset 35 with the currently used 20-km resolution (Fig. 4), we consider a set of 13 ice-shelf groups and determine the area-averaged basal melt for each group from the data of Rignot et al. (2013). The definition of these groups along with the calculated average melt rates are shown in Fig. 7. Note that the shelves have been grouped based on their geographical location, but also for more practical reasons such as the possibility of distinguishing their boundaries on the 20-km grid.

As a starting point for constructing the effective ocean temperature, we consider the observational data of the World Ocean 40 Atlas 2013 (WOA13, Locarnini et al. 2013), which contains a global dataset of ocean temperatures within a range of depths (0–5500 m). Restricting ourselves to the temperature data for latitudes south of 60°S, we average the ocean temperatures over depth intervals  $[z_1, z_2]$ , where  $z_1$  is the level of the bed (i.e. the deepest level for which data is available) with the additional constraint  $z_1 \geq -1000$  m, and  $z_2 = \min\{0, z_1 + 400\text{ m}\}$ . This results in a relatively smooth 2-D temperature field containing 45 an inherent dependence on the bottom topography, which can be considered a first estimate for the ocean water flowing into the ice-shelf cavities. One should note that the details of the depth averaging are rather arbitrary as we will soon modify the 50



Ice-shelf group	Average basal melt ( $\text{m yr}^{-1}$ )
1 <i>Filchner, Ronne</i>	$0.32 \pm 0.08$
2 <i>Stancomb, Brunt, Riiser-Larsen, Quar, Ekström, Atka</i>	$0.2 \pm 0.1$
3 <i>Jelbart, Fimbul, Vigrid, Nivl, Lazarev, Borchgrevink, Baudoin, Prince Harald, Shirase</i>	$0.5 \pm 0.1$
4 <i>Amery, Publications</i>	$0.6 \pm 0.4$
5 <i>West</i>	$1.7 \pm 0.7$
6 <i>Shackleton, Tracy, Tremechus, Conger</i>	$2.7 \pm 0.5$
7 <i>Totten, Moscow University, Holmes</i>	$7.1 \pm 0.5$
8 <i>Mertz, Ninis, Cook East, Rennick, Lillie</i>	$1.7 \pm 0.4$
9 <i>Ross</i>	$0.12 \pm 0.07$
10 <i>Sulzberger, Swinburne, Nickerson, Land</i>	$1.5 \pm 0.2$
11 <i>Getz, Dotsen, Crosson, Thwaites, Pine Island, Cosgrove, Abbot, Ven-able</i>	$5.6 \pm 0.3$
12 <i>Stange, George VI, Bach, Wilkins</i>	$3.0 \pm 0.4$
13 <i>Larsen B-C-D-E-F-G</i>	$0.5 \pm 0.6$

**Figure 7.** The 13 groups of ice shelves used for constructing the effective ocean temperature field. Average melt rates and error estimates for each group are calculated from the data of Rignot et al. (2013) for individual ice shelves.

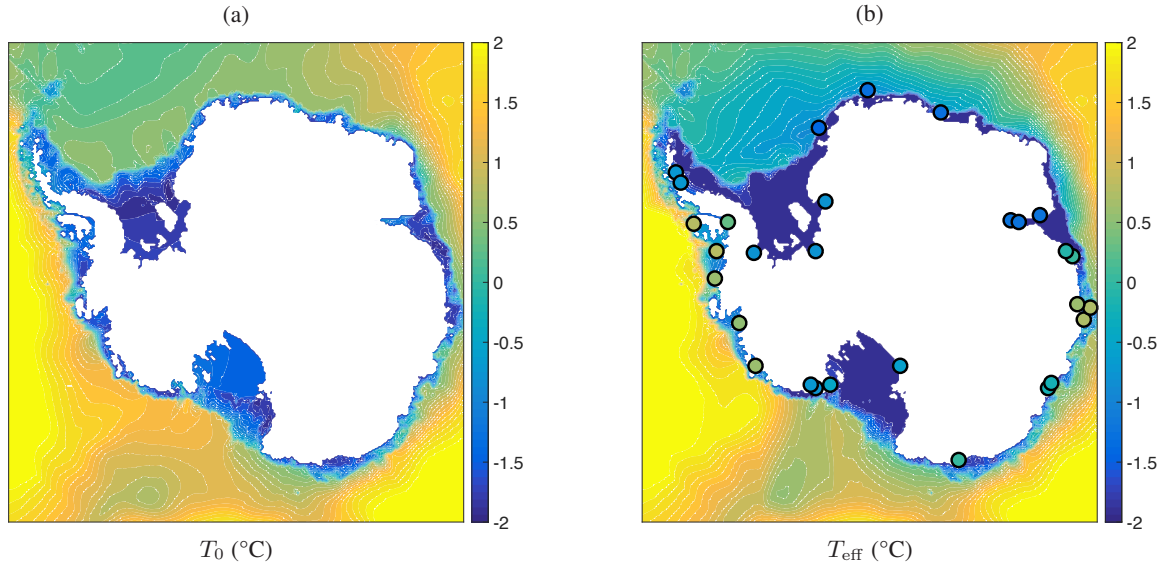


temperature field in order to obtain melt rates that agree with the data of Rignot et al. (2013). The depth-averaged temperature field is now remapped on the same 20-km grid as the topography data (see Section 2.3 and Fig. 4) and interpolated using natural-neighbour interpolation (i.e. a weighted version of nearest-neighbour interpolation, giving smoother results) to obtain data in the entire domain of interest. The resulting temperature field, called  $T_0$ , is shown in Fig. 8a.

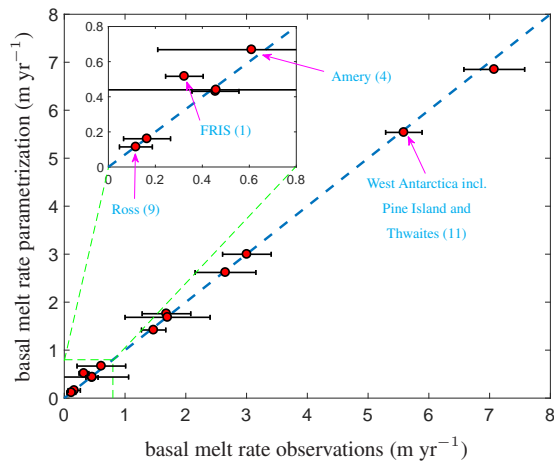
5 The aim is now to modify this depth-averaged, interpolated temperature field  $T_0$  in such a way that the basal melt parametrization yields melt rates close to those shown in Fig. 7 for each ice-shelf group. As explained earlier, this modification is necessary for eliminating biases in  $T_0$  caused by the sparse observations and numerical interpolation, and also because the flow dynamics of the ocean are not resolved. The field  $T_0$  is now modified by adding a 2-D field of temperature differences ( $\Delta T$ ), which, in turn, is the result of linearly interpolating individual values of  $\Delta T$  in 29 carefully chosen sample points, with  $\Delta T = 0$  on 10 the domain boundary. The resulting effective temperature field,  $T_{\text{eff}} = T_0 + \Delta T$ , is shown in Fig. 8b, which also indicates the positions of the aforementioned sample points along with the used values of  $\Delta T$  in these points. Note that for technical reasons explained in Appendix A, we have applied a lower limit to the effective temperature equal to the pressure freezing point at 15 surface level. With the current choice  $S_a = 34.6$  psu, this implies  $T_{\text{eff}} \geq -1.9$  °C. Comparing Figs. 8a and b, we see that the main effect of  $\Delta T$  is a decrease in the ocean temperature over most of the continental shelf and most ice-shelf cavities (in particular for Ross and Amery ice shelves), and a slight increase in the ocean temperature in West Antarctica and some regions in East Antarctica (e.g. shelf group 6 in Fig. 7). Again, note that the details in the procedure for calculating  $T_0$  and  $\Delta T$  are somewhat arbitrary, since increasing one term would require decreasing the other term in order to obtain similar values for  $T_{\text{eff}}$  with similar basal melt rates.

Fig. 9 shows the basal melt rates computed by the parametrization using the effective temperature  $T_{\text{eff}}$  of Fig. 8b as forcing. 20 An area-averaged value is obtained for each of the 13 ice-shelf groups in Fig. 7 and compared with the observational values from the Rignot et al. (2013) data. By construction, the modelled basal melt rates correspond closely to the observational values and fall within the error estimates. A notable exception is the value for Filchner-Ronne ice shelf (FRIS), which is  $0.32 \pm 0.08$  m yr<sup>-1</sup> according to the observations, whereas the parametrization gives a value just above 0.5 m yr<sup>-1</sup>. This discrepancy is caused by the lower bound of  $-1.9$  °C imposed on the effective temperature. As we can see in Fig. 8b, the ocean water below 25 FRIS is almost entirely at this minimum temperature, making it impossible to further improve the basal melt rate without using unfeasibly low values for  $T_{\text{eff}}$ . The lower bound also has a physical meaning, as the inflow of ocean water into the ice-shelf cavities is unlikely to be much colder than the surface freezing point.

Nevertheless, the plume parametrization in conjunction with the constructed effective temperature field appears to yield 30 realistic present-day melt rates for all shelf groups. Therefore, we can conclude that the effective temperature shown in Fig. 8b is a realistic forcing field, at least within the current modelling framework. Clearly, this field contains an inherent dependence on the bottom topography, with typically lower temperatures above the continental shelves (and thus in the ice-shelf cavities), while still retaining the spatial variation in temperature of the surrounding deep ocean (e.g. higher temperatures for West-Antarctica, leading to higher melt rates for ice-shelf groups 11 and 12 as defined in Fig. 7).



**Figure 8.** (a) Depth-averaged and interpolated ocean temperature,  $T_0$ , calculated from WOA13 data. (b) Effective ocean temperature  $T_{\text{eff}} = \max\{T_0 + \Delta T, -1.9\}$  constructed from  $T_0$  as described in Section 3.2. The circles indicate the positions of the sample points in which the values of  $\Delta T$  are imposed. The colour of each circle corresponds to the imposed value of  $\Delta T$  (same colour scale), ranging from  $-1.4^{\circ}\text{C}$  to  $0.8^{\circ}\text{C}$ . The full  $\Delta T$  field is obtained by linearly interpolating these values.



**Figure 9.** Area-averaged basal melt rates for each ice-shelf group in Fig. 7 obtained with the plume parametrization and the effective temperature field of Fig. 8b. The modelled melt rates are plotted against the averaged observational values given in Fig. 7. For four important shelf groups, the data points are explicitly labelled along with the corresponding group number in Fig. 7.



### 3.3 Comparison of 2-D melt-rate patterns

The effective grounding-line depth and effective slope in Fig. 4, the effective ocean temperature in Fig. 8b and the assumption  $S_a = 34.6$  psu constitute the full set of input parameters necessary for evaluating the plume parametrization on the entire 2-D geometry. The resulting 2-D field of basal melt rates under all Antarctic ice shelves is shown in Fig. 10a (note that this is the 5 same data used for the area-averaged melt rates in Fig. 9, but now plotted as a spatial field rather than averaged values over the ice shelves). A general pattern that can be observed, especially on the bigger ice shelves, consists of regions of higher melt close to the grounding line and lower melt or patches of refreezing closer to the ice front. This pattern is obviously a consequence of the underlying plume model, as shown in Section 3.1 for data along a flow line. Moreover, the highest melt rates occur 10 in West Antarctica (shelf groups 11 and 12) and some specific shelves in East Antarctica (shelf groups 6 and 7), where the effective temperature is significantly higher than elsewhere. This fact, along with the general melt pattern and the correlation with the surrounding ocean temperature, are in line with observations, e.g. Rignot et al. (2013). However, one should note that the Rignot et al. (2013) melt pattern shows a greater spatial variability, with more patches of (stronger) refreezing occurring 15 between patches of positive melt. The lack of such prominent patches of refreezing in the current parametrization might have different reasons, such as the coarse resolution or the fact that we disregard the details of the ocean circulation within the ice-shelf cavities, as well as effects due to stratification and the Coriolis force. All in all, the plume parametrization, together with the effective temperature field, appears to give a realistic melt pattern for Antarctica, showing both a large spatial variability and average melt rates that agree with observations.

For comparison, we also evaluate the quadratic parametrization of DeConto and Pollard (2016), described in Section 3.1, using the same geometric data and the effective temperature field of Fig. 8b as input. The resulting basal melt rate pattern is 20 shown in Fig. 10b. Comparing this figure to Fig. 10a immediately shows that the quadratic parametrization yields significantly lower melt rates than the plume parametrization, at least with the current effective temperature as input. The only visible patches of basal melt are located in the aforementioned regions where the ocean temperature is high, as well as near the grounding line of Filchner-Ronne ice shelf. Therefore, if the effective temperature in Fig. 8b is indeed characteristic of the true 25 temperatures in the ice-shelf cavities, the quadratic parametrization would require significant tuning in order to obtain a similar agreement with observed melt rates as currently found with the plume parametrization. For completeness, we mention that the linear parametrization of Beckmann and Goosse (2003) yields even lower melt rates due to its low temperature sensitivity, as discussed in Section 3.1.

To further clarify the differences between the two parametrizations in Fig. 10, we have repeated the steps outlined in Section 3.2 and constructed a second effective temperature field based on the quadratic parametrization by DeConto and Pollard 30 (2016) instead of the plume parametrization. The resulting temperature field is shown in Fig. 11a. Note that the difference between this field and the one in Fig. 8b only lies in the values chosen for  $\Delta T$  and not in the underlying interpolated observations ( $T_0$ ). For simplicity, the  $\Delta T$  values have been imposed in the same sample points as used for Fig. 8b. Comparing the two effective temperature fields in Figs. 8b and 11a shows that much higher ocean temperatures are required for the quadratic parametrization to give realistic area-averaged melt rates. The  $\Delta T$  values imposed in the sample points indicated in Fig. 11a

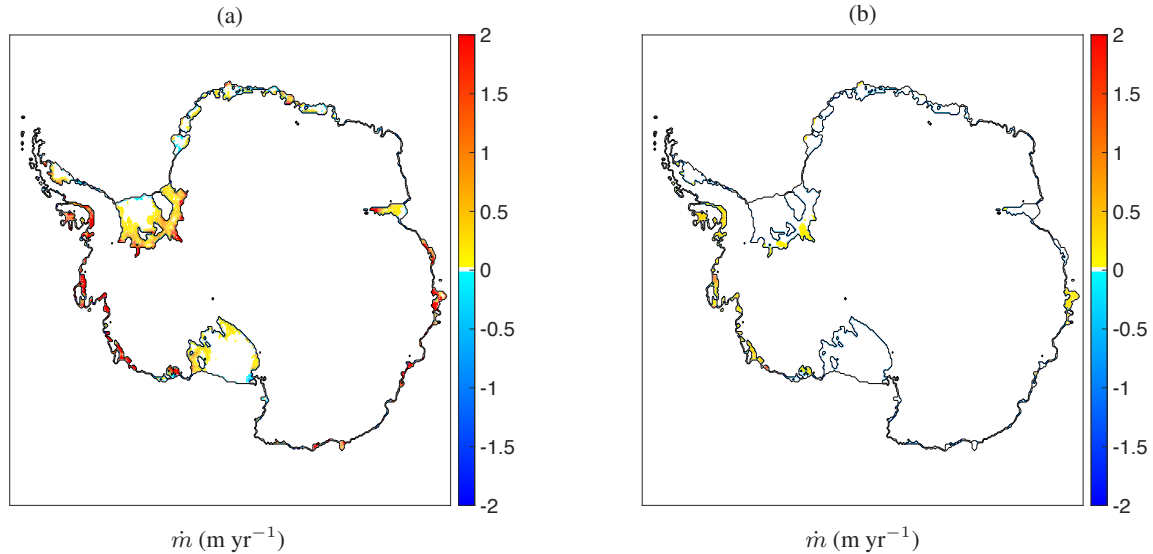


**Figure 10.** Basal melt rates in meter per year with the Bedmap2 topographic data and the effective temperature field of Fig. 8b as obtained from: (a) the plume parametrization with additional input parameters from Fig. 4; (b) the quadratic parametrization of DeConto and Pollard (2016).

range from  $-0.5$  °C to  $5.4$  °C, while those used for Fig. 8b range from  $-1.4$  °C to  $0.8$  °C. Furthermore, we can calculate the root mean square values of  $T_{\text{eff}} - T_0$  over the entire domain (disregarding the continental points), yielding  $0.3$  °C for Fig. 8b and  $1.1$  °C for Fig. 11a. Hence, the effective temperature in Fig. 8b lies closer to the underlying observational data  $T_0$  than the field in Fig. 11a.

5 The basal melt rates resulting from the quadratic parametrization and the new effective temperature field are shown in Fig. 11b. Clearly, the higher ocean temperatures cause significantly higher melt rates than those shown in Fig. 10b. However, compared with the plume parametrization in Fig. 10a, the spatial distribution of these melt rates is more uniform, showing less prominent melt peaks near grounding lines and no patches of refreezing. It appears that the quadratic temperature dependence together with the (slight) depth dependence through the pressure freezing point  $T_f$  (equation (1b)) is not sufficient for obtaining  
 10 realistic melt rates without significantly increasing the input ocean temperature, which can be considered equivalent to using different tuning factors for different ice shelves. On the other hand, the plume parametrization, containing an additional geometry dependence through the grounding-line depth and local slope, appears to yield the required melt rates rather naturally with only a minimal tuning of the observed ocean temperatures, and it results in a more realistic spatial pattern with highest basal melt rates near the grounding line as well as areas of refreezing.

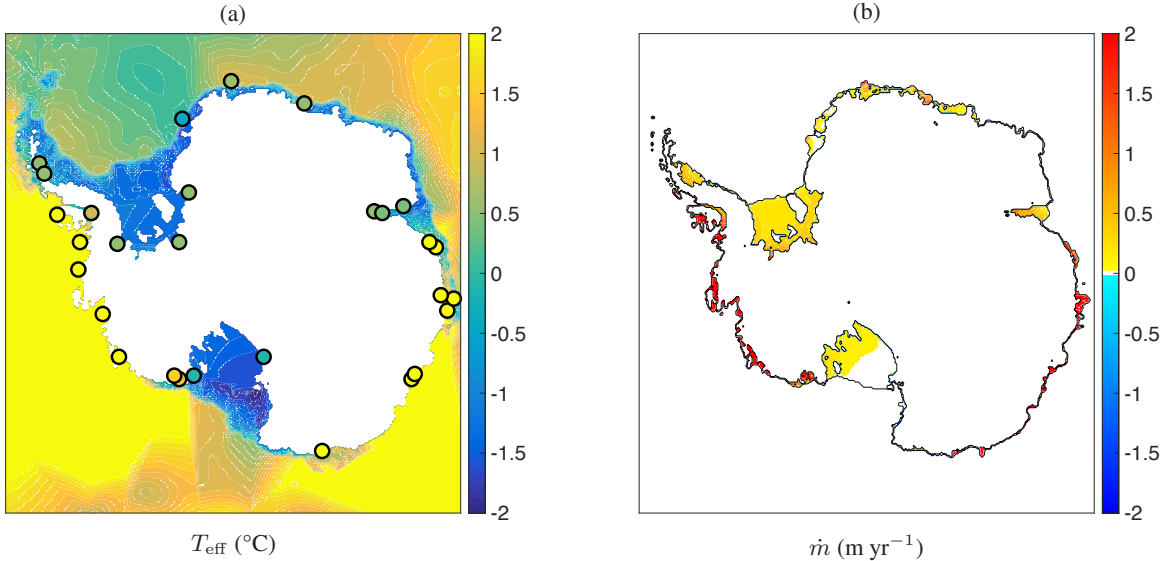


**Figure 11.** (a) Effective temperature field constructed in a similar way as Fig. 8b, but with different values for  $\Delta T$  (indicated by the circles and ranging from  $-0.5^{\circ}\text{C}$  to  $5.4^{\circ}\text{C}$ ), chosen in order to match the melt rates of the quadratic parametrization of DeConto and Pollard (2016) with the data of Rignot et al. (2013). (b) Basal melt rates obtained with the quadratic parametrization of DeConto and Pollard (2016) using the Bedmap2 topographic data and the effective temperature in (a) as input.

#### 4 Conclusions

In this study, we have presented the application of a basal melt parametrization, based on the dynamics of buoyant meltwater plumes, to all ice shelves in Antarctica. The physical basis of this parametrization is the plume model of Jenkins (1991), which describes the fluxes of mass, momentum, heat and salinity within a meltwater plume travelling up from the grounding line 5 along the ice-shelf base. Details of the proposed parametrization have been discussed in earlier works (Jenkins, 2011, 2014) for idealized one-dimensional geometries along an ice-shelf flow line. In particular, the basal melt rate given by the plume model follows a rather universal scaling law depending on the ice-shelf geometry (basal depth  $z_b$ , local slope angle  $\alpha$ , and grounding-line depth  $z_{gl}$ ) as well as the ambient ocean temperature  $T_a$  and the pressure freezing point  $T_f$ .

Here, the plume parametrization has been tested for two realistic ice-shelf geometries along a flow line and, for the first time, 10 applied to a completely two-dimensional geometry covering all the Antarctic ice shelves. The one-dimensional tests along flow lines of Filchner-Ronne and Ross ice shelves (Section 3.1) reveal the typical characteristics of the parametrization, namely higher melt rates near the grounding line and in regions of high basal slope. Patches of refreezing can occur further away from the grounding line. Moreover, the plume parametrization exhibits a nonlinear dependence on the ocean temperature, and the increase in melting resulting from higher ocean temperature is dependent on the ice-shelf geometry. In contrast, simpler



parametrizations based solely on the local balance of heat at the ice-ocean interface are not able to capture the complex melt pattern nor the temperature sensitivity.

Applying the essentially one-dimensional plume parametrization to a two-dimensional geometry is not trivial and, ideally, it would require a detailed knowledge of both the ice-shelf geometry and the ocean circulation in the ice-shelf cavities. The 5 method discussed in Section 2.3 provides a solution to these issues by constructing a field of effective grounding-line depths and slope angles for each shelf point from topographic data. The resulting values for  $z_{gl}$  and  $\alpha$  can be interpreted as reflecting the average effect of all plumes that reach the shelf point. This method provides a straightforward way to extend the parametrization from 1-D to 2-D for a given topography and ice mask, but it is not unique. For example, it does not directly take into account the horizontal distance from an ice-shelf point to the grounding line (an alternative method presented in Appendix B does take 10 this distance into account, without improving the results).

However, since the temperature sensitivity of the plume parametrization can be considerable, a more important factor for the two-dimensional model is finding an ocean temperature field that is characteristic for the ocean water flowing into the ice-shelf cavities. In this respect, the results in Sections 3.2 and 3.3 show that the depth-averaged and interpolated data from 15 observations only need a minimal offset  $\Delta T$  (between  $-1.4$  °C and  $0.8$  °C) in order to obtain an effective temperature  $T_{\text{eff}}$  (Fig. 8b) with which the plume parametrization gives basal melt rates close to the present-day observations of Rignot et al. (2013). In contrast, a much higher offset  $\Delta T$  (between  $-0.5$  °C to  $5.4$  °C) is required for obtaining the same melt rates with the quadratic parametrization of DeConto and Pollard (2016), as shown in Fig. 11. The latter behaviour is also apparent in Pollard and DeConto (2012), where different tuning factors in the basal melt parametrization are used for different sectors along 20 the Antarctic coastline, and in DeConto and Pollard (2016), where offsets of  $3$  °C and  $5$  °C are added to the ocean temperature in the Amundsen and Bellinghausen seas (resulting from an ocean model) in order to obtain the correct present-day basal melt rates and grounding-line retreat.

All in all, the presented plume parametrization, together with the constructed effective temperature field, gives realistic 25 results for the present-day basal melt in Antarctica, both in terms of area-averaged values (Fig. 9) and the spatial pattern (Fig. 10a). The inherent geometry dependence, based on the plume dynamics, gives a more natural spatial variation that cannot be captured with local heat-balance models, a major aspect being the occurrence of refreezing. Of course, the current discussion only assumes a steady state regarding the ice dynamics and the ocean temperature. The question remains how an ice-dynamical model would behave when coupled to the plume parametrization, both for present-day forcing and for a varying climate. As a next step, it is important to perform such transient simulations of an ice model coupled to the plume parametrization and 30 conduct sensitivity experiments. For such simulations, the effective temperature in Fig. 8b, even though it is a constructed field, can prove to be a valuable reference state to which temperature anomalies can be added. Eventually, coupled ice-ocean simulations (e.g. DeConto and Pollard 2016) can benefit from this approach by comparing ocean-model output to this reference state.



## Appendix A: Details of the basal melt parametrization

Here we present more details of the basal melt parametrization summarized in Section 2.2. For a given point at the ice-shelf base with local depth  $z_b$  and local slope angle  $\alpha$ , we can determine the corresponding grounding-line depth  $z_{gl}$  and ambient ocean properties  $T_a$  and  $S_a$ . As summarized in Table 1, these quantities, together with a set of constant parameters, serve as the input of the parametrization. The basal melt rate  $\dot{m}$  in meter per year at the particular ice-shelf point is now calculated as follows. First we define the characteristic freezing point:

$$T_f = \lambda_1 S_a + \lambda_2 + \lambda_3 z_{gl}, \quad (\text{A1})$$

and an effective heat exchange coefficient:

$$\Gamma_{TS} = \Gamma_T \left( 0.545 + 3.5 \times 10^{-5} \cdot \frac{T_a - T_f}{\lambda_3} \cdot \frac{E_0 \sin \alpha}{\Gamma_{TS0} + E_0 \sin \alpha} \right) \quad (\text{A2})$$

10 The melt scale  $M$  in meter per year is now calculated from:

$$M = 10 \cdot (T_a - T_f)^2 \left( \frac{\sin \alpha}{C_d + E_0 \sin \alpha} \right)^{1/2} \left( \frac{\Gamma_{TS}}{\Gamma_{TS} + E_0 \sin \alpha} \right)^{1/2} \left( \frac{E_0 \sin \alpha}{\Gamma_{TS} + E_0 \sin \alpha} \right). \quad (\text{A3})$$

The length scale  $l$  is given by:

$$l = \frac{T_a - T_f}{\lambda_3} \cdot \frac{x_0 \Gamma_{TS} + E_0 \sin \alpha}{x_0 (\Gamma_{TS} + E_0 \sin \alpha)}, \quad (\text{A4})$$

where the second factor provides a slope-dependent scaling of the point of transition between melting ( $\dot{m} > 0$ ) and refreezing ( $\dot{m} < 0$ ), with  $x_0 = 0.56$  (see Fig. 2). We can now determine the dimensionless coordinate:

$$\hat{X} = \frac{z_b - z_{gl}}{l}, \quad (\text{A5})$$

and calculate the basal melt rate from:

$$\dot{m} = M \cdot \hat{M}(\hat{X}), \quad (\text{A6})$$

where  $\hat{M}(\hat{X})$  is the dimensionless melt curve shown in Fig. 2 and given by the following polynomial function:

$$20 \quad \hat{M}(\hat{X}) = \sum_{k=0}^{11} p_k \hat{X}^k, \quad (\text{A7})$$

for which the coefficients  $p_k$  are given in Table A1.

Note that we require  $0 \leq \hat{X} \leq 1$  in order to remain within the valid domain of the polynomial fit and avoid unbounded values of  $\hat{M}$ . It is rather straightforward to show that  $\hat{X} \leq 1$  is guaranteed for  $T_a \geq \lambda_1 S_a + \lambda_2$ , i.e. the ocean temperature should be above the freezing point at surface level ( $z = 0$ ). By combining equations (A1), (A4) and (A5) and taking the limit 25  $T_a \rightarrow \lambda_1 S_a + \lambda_2$ , we obtain  $\hat{X} \rightarrow (1 - z_b/z_{gl})F^{-1}$ , where  $F$  denotes the second (slope-dependent) factor in (A4). Because all the terms appearing in this factor  $F$  are positive and  $x_0 < 1$ , we have  $F \geq 1$ . Together with  $z_{gl} \leq z_b \leq 0$ , this implies  $\hat{X} \leq 1$  in this particular limit for the ocean temperature. Since  $T_a$  appears in the denominator of  $\hat{X}$  in (A5), ocean temperatures above this limit will yield smaller values for  $\hat{X}$ . Hence, the  $\hat{X} \leq 1$  is guaranteed for  $T_a \geq \lambda_1 S_a + \lambda_2$ . Note that this is the reason why we have applied this lower limit to the effective temperature  $T_{\text{eff}}$  in Fig. 8b.



**Table A1.** Coefficients for the polynomial fit of the dimensionless melt curve  $\hat{M}(\hat{X})$ .

$p_{11}$	$6.388 \times 10^4$
$p_{10}$	$-3.521 \times 10^5$
$p_9$	$8.467 \times 10^5$
$p_8$	$-1.166 \times 10^6$
$p_7$	$1.015 \times 10^6$
$p_6$	$-5.820 \times 10^5$
$p_5$	$2.219 \times 10^5$
$p_4$	$-5.564 \times 10^4$
$p_3$	$8.927 \times 10^3$
$p_2$	$-8.952 \times 10^2$
$p_1$	$5.528 \times 10^1$
$p_0$	$1.371 \times 10^{-1}$

## Appendix B: Alternative algorithm for finding the grounding-line depths and slopes

In Section 2.3 we presented an algorithm for determining the effective grounding-line depth  $z_{gl}$  and effective slope angle  $\alpha$ , which is necessary for applying the plume parametrization to two-dimensional ice-shelf geometries. Clearly, this algorithm is not unique. Here we present an alternative for calculating both quantities, which will give slightly different results for the effective temperature and basal melt rates.

The original algorithm of Section 2.3 calculates both  $z_{gl}$  and  $\alpha$  from the average over multiple “valid” directions. Although this is a simple way to account for multiple plume directions, one could argue that it might suppress the effects of high local gradients and of plumes coming from greater depths. Therefore, an alternative for calculating the local slope at shelf point  $(i,j)$  would simply be the local gradient of the ice-shelf base:

$$10 \quad \tan[\alpha(i,j)] = |\nabla z_b| = \sqrt{\left(\frac{\partial z_b}{\partial x}\right)^2 + \left(\frac{\partial z_b}{\partial y}\right)^2}. \quad (B1)$$

Furthermore, the effective grounding-line depth can be determined from a modified version of (12a):

$$z_{gl}(i,j) = \frac{\sum_{\text{valid } n} w_n(i,j) d_n(i,j)}{\sum_{\text{valid } n} w_n(i,j)}, \quad (B2)$$

where  $w_n(i,j)$  is a weight factor equal to the *overall slope* between the shelf point at depth  $z_b(i,j)$  and the grounding line at depth  $d_n(i,j)$  in the  $n$ -th direction:

$$15 \quad w_n(i,j) = \frac{z_b(i,j) - d_n(i,j)}{l_n(i,j)}, \quad (B3)$$

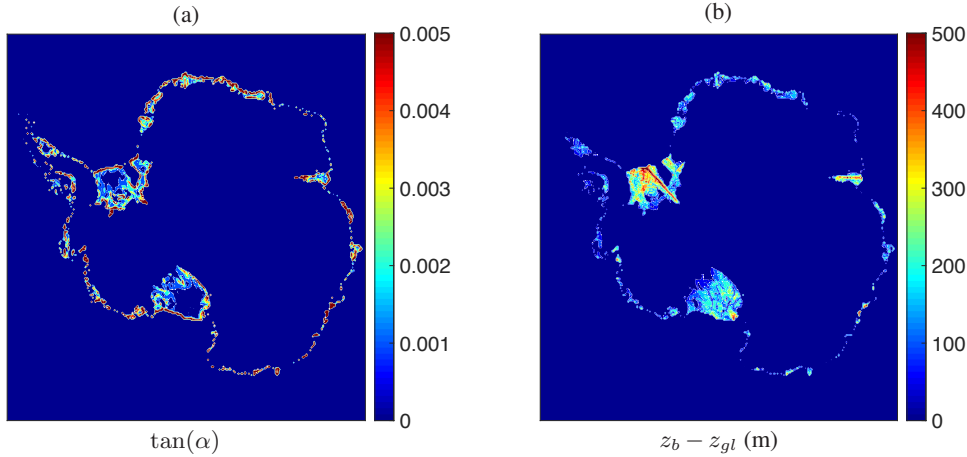


**Figure A1.** Effective plume paths under the Antarctic ice shelves as calculated by the modified algorithm of Appendix B using the Bedmap2 topographic data remapped on a 20 km by 20 km grid. (a) The slope  $\tan(\alpha)$  equal to the local gradient. (b) The difference between local ice-base depth and associated grounding-line depth,  $z_b - z_{gl}$ .

with  $l_n(i, j)$  denoting the horizontal distance between the shelf point  $(i, j)$  and the corresponding grounding-line point in the  $n$ -th direction. Hence, relatively deep grounding-line points that are close to the shelf point will have a larger weight factor than relatively shallow grounding-line points that are far away. Apart from the modifications in (B1)-(B3), the algorithm is evaluated as described in Section 2.3. The plume paths resulting from the modified algorithm, using the same topography data 5 (Bedmap2) as in Section 2.3, are shown in Fig. A1, which should be compared with Fig. 4. Clearly, using the local gradient of the ice-shelf base leads to higher values of the slope, especially near the ice-shelf edges. Furthermore, we generally obtain higher values for  $z_b - z_{gl}$ , indicating that deeper grounding-line points are given a larger weight, as expected. Interestingly, Fig. A1b contains clearly visible straight paths coming from the deepest grounding lines on Filchner-Ronne and Amery ice shelves, which might be an undesirable artefact.

10 The fields in Fig. A1 can now be used as input for the plume parametrization. We repeat the calculations described in Sections 3.2 and 3.3 in order to find an effective ocean temperature field (Fig. A2a) with which the plume parametrization gives average melt rates that agree with the observational data of Rignot et al. (2013) as closely as possible. Moreover, the resulting two-dimensional field of basal melt rates is shown in Fig. A2b. The new effective temperature is generally lower than the original field in Fig. 8b, with  $\Delta T$  values in the sample points ranging from  $-2.1$  °C to  $0.4$  °C (compared with  $-1.4$  °C to 15  $0.8$  °C for Fig. 8b). The new melt-rate pattern is qualitatively similar to Fig. 10a, although the melt rates close to the grounding lines appear to be considerably higher. In fact, the resulting average melt rates for Filchner-Ronne and Amery ice shelves are  $1.3$  m yr $^{-1}$  and  $1.8$  m yr $^{-1}$ , respectively, which significantly overestimate the observational values of Rignot et al. (2013) (see Fig. 7). These estimates cannot be improved by further decreasing the effective temperature, because the values of  $T_{eff}$  in these regions are already at the lower bound of  $-1.9$  °C. Note that this problem is similar to the (slight) overestimation of the melt

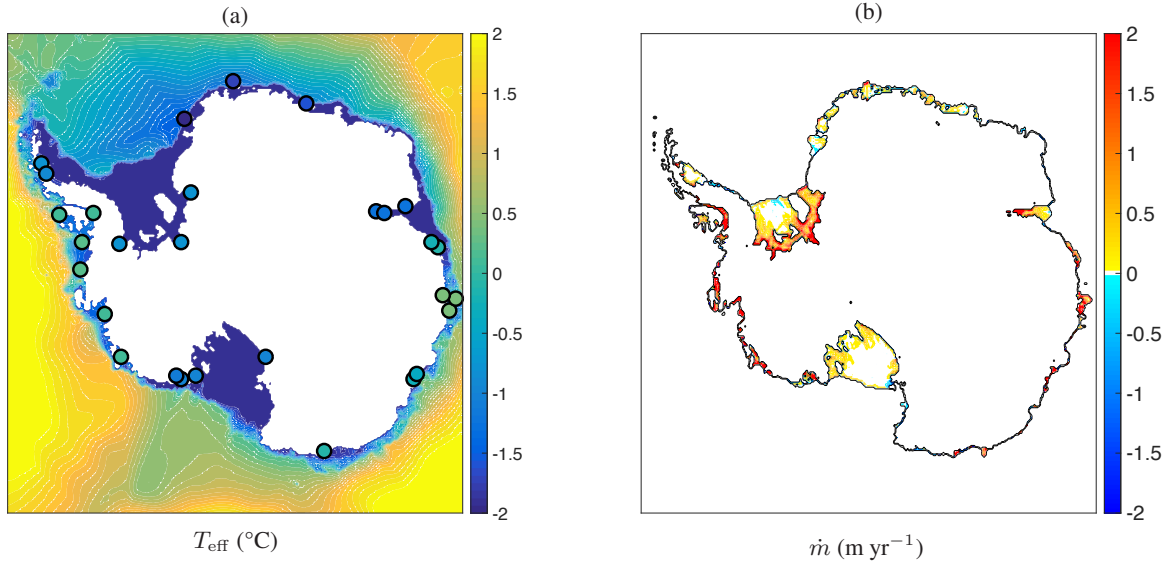


**Figure A2.** (a) Effective temperature field constructed in a similar way as Fig. 8b, but with different values for  $\Delta T$  (indicated by the circles and ranging from  $-2.1\text{ }^{\circ}\text{C}$  to  $0.4\text{ }^{\circ}\text{C}$ ), chosen in order to match the melt rates of the plume parametrization with the modified algorithm (Appendix B) with the data of Rignot et al. (2013). (b) Basal melt rates obtained with the modified parametrization using the Bedmap2 topographic data and the effective temperature in (a) as input.

rates for Filchner-Ronne ice shelf with the original algorithm, as discussed in Section 3.2. Thus, using the modified algorithm for  $z_{gl}$  and  $\alpha$  clearly has an effect on the calculated melt rates, but the results in Fig. A2b are not a clear improvement over those in Fig. 10a. Further tests would be necessary in order to clarify which algorithm is best suited for e.g. simulations with dynamical ice models.

5 *Competing interests.* The authors declare that they have no conflict of interest.

*Acknowledgements.* Financial support for W.M.J. Lazeroms was provided by the Netherlands Organisation of Scientific Research (NWO-ALW-Open 824.14.003).



## References

Beckmann, A. and Goosse, H.: A parameterization of ice shelf-ocean interaction for climate models, *Ocean modelling*, 5, 157–170, 2003.

Bo Pedersen, F.: Dense bottom currents in rotating ocean, *J. Hydraul. Div. Amer. Soc. Civ. Eng.*, 106, 1291–1308, 1980.

Bombosch, A. and Jenkins, A.: Modeling the formation and deposition of frazil ice beneath Filchner-Ronne Ice Shelf, *J. Geophys. Res. Oceans*, 100, 6983–6992, 1995.

De Boer, B., Dolan, A. M., Bernales, J., Gasson, E., Goelzer, H., Golledge, N., Sutter, J., Huybrechts, P., Lohmann, G., Rogozhina, I., Abe-Ouchi, A., Saito, F., and van de Wal, R.: Simulating the Antarctic ice sheet in the Late-Pliocene warm period: PLISMIP-ANT, an ice-sheet model intercomparison project, *The Cryosphere*, 9, 881–903, 2015.

DeConto, R. M. and Pollard, D.: Contribution of Antarctica to past and future sea-level rise, *Nature*, 531, 591–597, 2016.

Depoorter, M. A., Bamber, J. L., Griggs, J. A., Lenaerts, J. T. M., Ligtenberg, S. R. M., Van den Broeke, M. R., and Moholdt, G.: Calving fluxes and basal melt rates of Antarctic ice shelves, *Nature*, 502, 89–92, 2013.

Ellison, T. H. and Turner, J. S.: Turbulent entrainment in stratified flows, *J. Fluid Mech.*, 6, 423–448, 1959.

Fretwell, P., Pritchard, H. D., Vaughan, D. G., Bamber, J. L., Barrand, N. E., Bell, R., Bianchi, C., Bingham, R. G., Blankenship, D. D., Casassa, G., Catania, G., Callens, D., Conway, H., Cook, A. J., Corr, H. F. J., Damaske, D., Damm, V., Ferraccioli, F., Forsberg, R., Fujita, S., Gim, Y., Gogineni, P., Griggs, J. A., Hindmarsh, R. C. A., Holmlund, P., Holt, J. W., Jacobel, R. W., Jenkins, A., Jokat, W., Jordan, T., King, E. C., Kohler, J., Krabill, W., Riger-Kusk, M., Langley, K. A., Leitchenkov, G., Leuschen, C., Luyendyk, B. P., Matsuoka, K., Mouginot, J., Nitsche, F. O., Nogi, Y., Nost, O. A., Popov, S. V., Rignot, E., Rippin, D. M., Rivera, A., Roberts, J., Ross, N., Siegert, M. J., Smith, A. M., Steinhage, D., Studinger, M., Sun, B., Tinto, B. K., Welch, B. C., Wilson, D., Young, D. A., Xiangbin, C., and Zirizzotti, A.: Bedmap2: improved ice bed, surface and thickness datasets for Antarctica, *The Cryosphere*, 7, 375–393, 2013.

Golledge, N. R., Kowalewski, D. E., Naish, T. R., Levy, R. H., Fogwill, C. J., and Gasson, E. G. W.: The multi-millennial Antarctic commitment to future sea-level rise, *Nature*, 526, 421–425, 2015.

Holland, D. M. and Jenkins, A.: Modeling thermodynamic ice-ocean interactions at the base of an ice shelf, *J. Phys. Oceanogr.*, 29, 1787–1800, 1999.

Holland, P. R., Jenkins, A., and Holland, D. M.: The response of ice shelf basal melting to variations in ocean temperature, *J. Clim.*, 21, 2558–2572, 2008.

Jenkins, A.: A one-dimensional model of ice shelf-ocean interaction, *J. Geophys. Res. Oceans*, 96, 20 671–20 677, 1991.

Jenkins, A.: Convection-driven melting near the grounding lines of ice shelves and tidewater glaciers, *J. Phys. Oceanogr.*, 41, 2279–2294, 2011.

Jenkins, A.: Scaling laws for the melt rate and overturning circulation beneath ice shelves derived from simple plume theory, in: EGU General Assembly 2014, vol. 16 of *Geophysical Research Abstracts*, EGU2014-13755, 2014.

Jenkins, A., Nicholls, K. W., and Corr, H. F. J.: Observation and parameterization of ablation at the base of Ronne Ice Shelf, Antarctica, *J. Phys. Oceanogr.*, 40, 2298–2312, 2010.

Lane-Serff, G. F.: On meltwater under ice shelves, *J. Geophys. Res. Oceans*, 100, 6961–6965, 1995.

Locarnini, R. A., Mishonov, A. V., Antonov, J. I., Boyer, T. P., Garcia, H. E., Baranova, O. K., Zweng, M. M., Paver, C. R., Reagan, J. R., Johnson, D. R., Hamilton, M., and Seidov, D.: World Ocean Atlas 2013, Volume 1: Temperature, NOAA Atlas NESDIS, 73, 2013.

MacAyeal, D. R.: Evolution of tidally triggered meltwater plumes below ice shelves, in: *Oceanology of the Antarctic Continental Shelf*, edited by Jacobs, S., pp. 133–143, American Geophysical Union, 1985.



Magorrian, S. J. and Wells, A. J.: Turbulent plumes from a glacier terminus melting in a stratified ocean, *J. Geophys. Res. Oceans*, 121, 4670–4696, 2016.

McPhee, M. G.: Turbulent heat flux in the upper ocean under sea ice, *J. Geophys. Res. Oceans*, 97, 5365–5379, 1992.

McPhee, M. G., Kottmeier, C., and Morison, J. H.: Ocean heat flux in the central Weddell Sea during winter, *J. Phys. Oceanogr.*, 29, 1166–1179, 1999.

5 Morton, B. R., Taylor, G., and Turner, J. S.: Turbulent gravitational convection from maintained and instantaneous sources, *Proc. R. Soc. Lond. A*, 234, 1–23, 1956.

Paolo, F. S., Fricker, H. A., and Padman, L.: Volume loss from Antarctic ice shelves is accelerating, *Science*, 348, 327–331, 2015.

Pollard, D. and DeConto, R. M.: Description of a hybrid ice sheet-shelf model, and application to Antarctica, *Geosci. Model Dev.*, 5, 1273–1295, 2012.

Pritchard, H. D., Arthern, R. J., Vaughan, D. G., and Edwards, L. A.: Extensive dynamic thinning on the margins of the Greenland and Antarctic ice sheets, *Nature*, 461, 971–975, 2009.

Pritchard, H. D., Ligtenberg, S. R. M., Fricker, H. A., Vaughan, D. G., Van den Broeke, M. R., and Padman, L.: Antarctic ice-sheet loss driven by basal melting of ice shelves, *Nature*, 484, 502–505, 2012.

15 Reerink, T. J., van de Berg, W. J., and van de Wal, R. S. W.: OBLIMAP 2.0: a fast climate model–ice sheet model coupler including online embeddable mapping routines, *Geosci. Model Dev.*, 9, 4111–4132, 2016.

Rignot, E., Jacobs, S., Mouginot, J., and Scheuchl, B.: Ice-shelf melting around Antarctica, *Science*, 341, 266–270, 2013.

Ritz, C., Edwards, T. L., Durand, G., Payne, A. J., Peyaud, V., and Hindmarsh, R. C. A.: Potential sea-level rise from Antarctic ice-sheet instability constrained by observations, *Nature*, 528, 115–118, 2015.

20 Shabtaie, S. and Bentley, C. R.: West Antarctic ice streams draining into the Ross Ice Shelf: configuration and mass balance, *J. Geophys. Res. Solid Earth*, 92, 1311–1336, 1987.